Uncovered bathymetry under Antarctica's fourth largest ice shelf reveals potential for seasonal warm water inflow

Hannes Eisermann

heiserma@awi.de

Alfred Wegener Institute https://orcid.org/0000-0002-5604-6484

Antonia Ruppel

Federal Institute for Geosciences and Natural Resources https://orcid.org/0000-0001-5101-411X

Tore Hattermann

Norwegian Polar Institute https://orcid.org/0000-0002-5538-2267

Kenichi Matsuoka

Norwegian Polar Institute https://orcid.org/0000-0002-3587-3405

Steven Franke

Alfred Wegener Institute Helmholtz Centre for Polar and Marine Research https://orcid.org/0000-0001-8462-4379

Elin Darelius

University of Bergen and Bjerknes Centre for Climate Research https://orcid.org/0000-0003-3060-0317

Felix Johann

Technical University of Darmstadt

Garrett Finucane

University of California, Los Angeles

Veit Helm

Alfred Wegener Institute https://orcid.org/0000-0001-7788-9328

Daniel Steinhage

Alfred Wegner Institute https://orcid.org/0000-0003-4737-9751

Stefan Leinen

Technical University of Darmstadt

Andreas Läufer

Federal Institute for Geosciences and Natural Resources https://orcid.org/0000-0003-2219-0450

Graeme Eagles

Alfred Wegener Institute

Article

Keywords:

Posted Date: April 4th, 2025

DOI: https://doi.org/10.21203/rs.3.rs-6328160/v1

Additional Declarations: There is **NO** Competing Interest.

Uncovered bathymetry under Antarctica's fourth largest ice shelf reveals potential for seasonal warm water inflow

Authors:

H. Eisermann[1], A. Ruppel[2], T. Hattermann[3,4], K. Matsuoka[3], S. Franke[5], E. Darelius[6], F. Johann[7], G. Finucane[8], V. Helm[1], D. Steinhage[1], S. Leinen[7], A. Läufer[2], G. Eagles[1]

Affiliations:

[1] Alfred Wegener Institute Helmholtz Centre for Polar and Marine Research, Bremerhaven, Germany.

[2] Federal Institute for Geosciences and Natural Resources, Hannover, Germany.

[3] Norwegian Polar Institute, Tromsø, Norway.

[4] University of Tromsø, Tromsø, Norway.

[5] Department of Geosciences, Tübingen University, Tübingen, Germany.

[6] Geophysical Institute, University of Bergen and Bjerknes Centre for Climate Research, Bergen, Norway.

[7] Technical University of Darmstadt, Darmstadt, Germany.

[8] University of California, Los Angeles, United States of America.

Corresponding Author:

H. Eisermann, heiserma@awi.de

Abstract

Interactions of ice and ocean around Antarctica determine the stability of ice shelves and the onshore ice masses they buttress. These interactions and the exchange of water between the open ocean and ice shelf cavities depend heavily on seabed morphology and depth. However, vast areas of the Antarctic margin remain bathymetrically undersampled, and some, including the cavity beneath the ~44,000 km^2 Riiser-Larsen Ice Shelf, Antarctica's fourth largest, were never yet visited. Here, we use new aerogeophysical and existing oceanographical data to infer bathymetry under the cavity and assess the interactions of ice, ocean and bed. We find a bed shaped by its setting at an extended continental margin, and modified by glacial processes. A 520 m-deep bathymetric gateway at the continental shelf break permits seasonal intrusion of Warm Deep Water into a subglacial trough that allows the warm water to reach the 1000 m deep grounding zone at the ice shelf's main inlet. The existence of analogous gateways at several ice shelves of Dronning Maud Land indicates that the buttressing effect on a large marine-based portion of the East Antarctic Ice Sheet, albeit whilst currently stable, may be approaching a serious tipping point with minimal changes to the oceanographic regime.

Introduction

The stability of Antarctic ice shelves is highly dependent on interactions at their interfaces. These interactions between the atmosphere, cryosphere, hydrosphere, and

45 lithosphere affect the overall mass balance of the Antarctic Ice Sheet by virtue of the
46 buttressing role played by the ice shelves[1]. Understanding and measuring ice shelf
47 processes is becoming more important because they are likely to change with global
48 warming, driving Antarctic contributions to the global sea level rise[2–4].
49
50 The primary mass loss process at Antarctica's ice shelves is basal melt[5]. Basal melt is
51 driven by oceanic heat in surface waters at the calving fronts and in deeper water
52 masses that penetrate into the cavities beneath the ice shelf base[6–8]. On seasonal and
53 climatic timescales, it varies along with the temperature and other properties of these
54 water masses.
55
56 Antarctica's fourth largest ice shelf, Riiser-Larsen with 44.000 km^2[(9)] (Fig. 1), is exposed
57 to the ocean along a 400 km wide calving front, behind which it is just about 110 km
58 long on average. Changes in the water mass properties it interacts with are largely
59 determined by the evolution and variability of the Weddell Gyre[10,11] (Fig. 1). The gyre
60 brings warmer sub-surface water from lower latitudes towards the continental
61 shelf[11,12]. Intrusion of this Warm Deep Water (WDW) into ice shelf cavities is largely
62 dependent on the relative depths of the WDW thermocline and the seabed beneath the
63 ice shelves. While the thermocline depth has been observed to undergo significant
64 seasonal changes here and at neighbouring ice shelves of Dronning Maud Land[13,14], the
65 seabed beneath the Riiser-Larsen Ice Shelf has never been surveyed bathymetrically.
66

67 To assess the present and future vulnerability of the Riiser-Larsen Ice Shelf to ocean
68 driven melt, we develop a new bathymetric model and interpret its implications for
69 regional circulation and ice shelf stability in the light of observed hydrography[13,15–17]
70 and the results of theoretical modelling. In a first step, the bathymetry beneath the ice
71 shelf is modelled based on newly acquired aerogeophysical data, using an inversion
72 of gravity data steered by known topography beneath grounded ice and open water,
73 and interpreted regional geology. Using the cavity map, oceanographic observations
74 along the coast, and newly acquired ice penetrating radar data (see Methods), we
75 estimate water and heat exchange between the open ocean and the ice shelf cavity with
76 its regional and seasonal variations. Finally, we use our findings to assess the ice shelf's
77 present and future stability in a regional context.

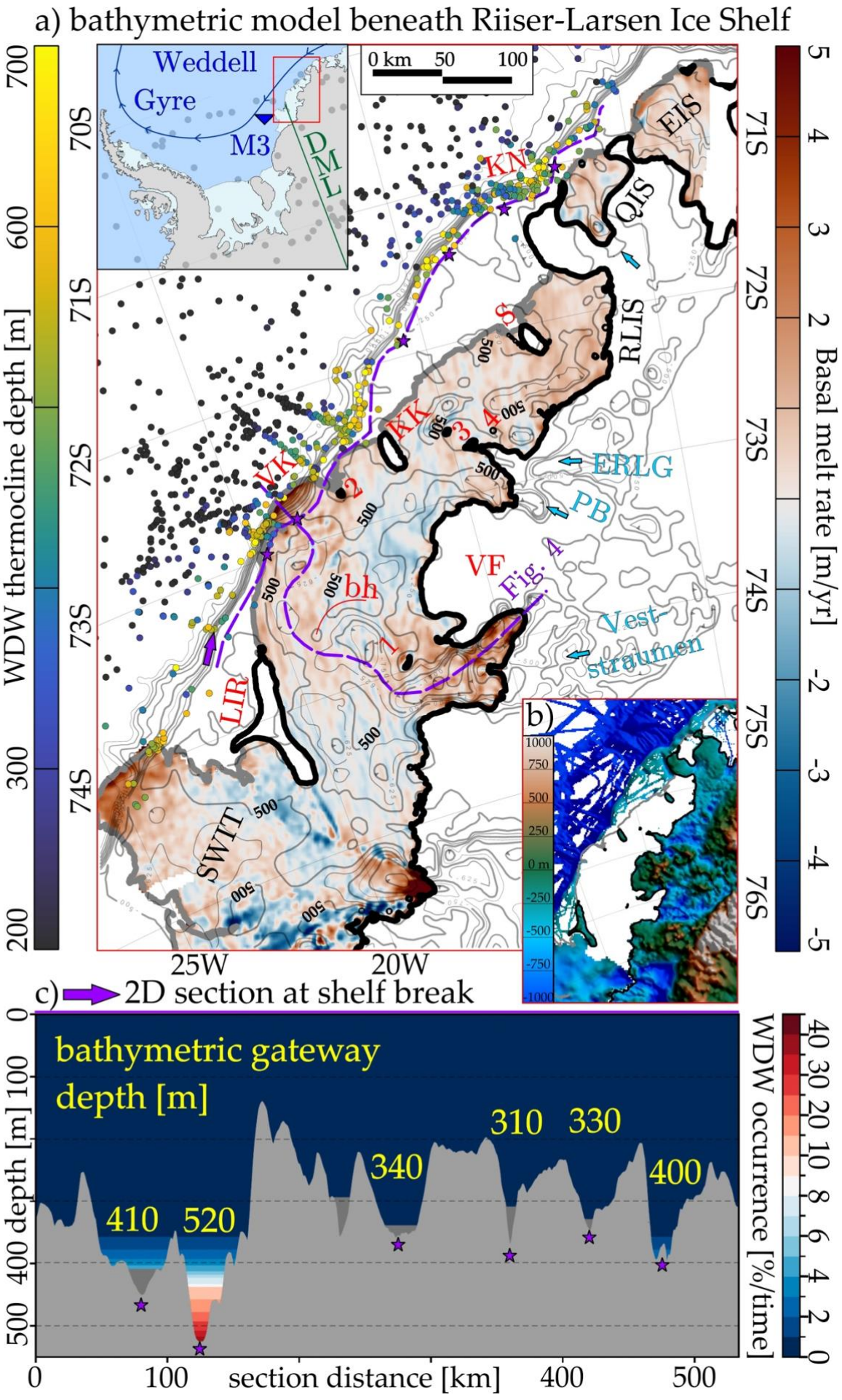
a) bathymetric model beneath Riiser-Larsen Ice Shelf
Weddell
Gyre
M3
DML
0 km 50 100
KN
KK
VK
bh
VF
Fig. 4
EIS
QIS
RLIS
ERLG
PB
Vest-
straumen
LIR
SWIT
1
2
3
4
500
b)
1000
750
500
250
0 m
-250
-500
-750
-1000
70S
71S
72S
73S
74S
71S
72S
73S
74S
75S
76S
25W
20W
WDW thermocline depth [m]
700
600
300
200
Basal melt rate [m/yr]
5
4
3
2
-2
-3
-4
-5
c) 2D section at shelf break
bathymetric gateway
depth [m]
410
520
340
310
330
400
depth [m]
0
100
400
500
0
100
section distance [km]
400
500
WDW occurrence [%/time]
40
30
20
10
8
6
4
2
0

Figure 1: Bathymetric model, oceanographic setting, and basal melt rates of the Riiser-Larsen Ice Shelf. Inset, upper left, shows the ice shelf's location in Dronning Maud Land (DML), East Antarctica, and the course of the coastal Weddell Gyre. (a) Bathymetric contours show the newly determined cavities of the Riiser-Larsen and Quar ice shelves based on gravity inversion performed in this study. Bold contours are shown for depths of 250, 500, 750, 1000, 1250, 1500, 1750, and 2000 m; lighter contours are shown for depths of 625 and 875 m. In the open ocean, coloured dots portray observed thermocline depths of Warm Deep Water from individual oceanographic profiles (see Methods). Across the region's ice shelves, average basal melt rates from 1997 to 2021[5] are portrayed. Calving fronts and grounded areas are extracted from MEaSUREs data collection[18] and additional databanks[19]. Blue arrows: glaciers (PB, Plogbreen; ERLG, eastern Riiser-Larsen Glacier), topographic features are labelled in red (KK, Kvitkuven; KN, Kapp Norvegia; LIR, Lyddan Ice Rise; 1, 2, 3, and 4, numbered pinning points; S, Skjoldet ice rise; VF, Vestfjella mountain site; VK, Vestkapp), and ice shelves in black (EIS, Ekström Ice Shelf; RLIS, Riiser-Larsen Ice Shelf; SWIT, Stancomb-Wills ice Tongue; QIS, Quar Ice Shelf). (b) Distribution of available shipborne bathymetric measurements[20], topography beneath grounded ice[21,22], Quar and Ekström cavity bathymetries from seismic measurements[22,23] and existing gravity modelling[24]. (c) Two-dimensional shelf break section along the purple line in (a) shows modelled bathymetry (grey) with colours in the background showing the percentage of time that WDW (T>-1.5C) was observed at a given depth at oceanographic mooring M3[17] located in the vicinity of the shelf break at a water depth of 738 m (for location see M3 in inset). Purple stars mark distinct gateways at depths of 300 m or deeper along the shelf break. Dark grey fills indicate shallower depths in shoreward reaches of the gateways, which block the potential route of inflowing WDW.

Results and discussion

Geological interpretation

Over the past decade, the method of inverting gravity anomalies towards sub-ice shelf bathymetry has been adapted and continually improved[25–28]. Still, it remains a major challenge to disentangle the signals of topographic height changes from those due to geological variability within the gravity data[29]. This is especially true across large gaps in the existing bathymetry, as encountered at the Riiser-Larsen Ice Shelf (Fig. 1b). The coarse spatial resolution (10 km) and low (10 mGal) accuracy of existing gravity data across the ice shelf[30] led to it being labelled 'challenging to invert' in Bed_AntGG2022, the only previous attempt to model the cavity[31]. Our model, in contrast, is based on newly acquired gravity data that are both more accurate (2.4 mGal) and spatially better resolved (up to 3.5 km) and benefits from a laterally varying density model based on a targeted geological interpretation (Fig. 2).

The gravity anomaly data (Fig. 2a) are first inverted towards bedrock density. At points of known bathymetry (Fig. 1b), this density can be taken as valid within our model domain since it is calculated to fit the gravity data. Using these points enables us to qualitatively interpret correlations between these well-constrained densities and characteristic associations in gravity, magnetic, and geological outcrop observations[32] (Figs. 2a-c). These allow us to extrapolate the inferred densities into less well constrained areas where bathymetry is unknown (Fig. 2d). Correlations include areas with high densities owing to the presence of Jurassic intrusions and a thick wedge of

126 basaltic lava flows (Explora Anomaly)[33,34] (Fig. 2c). Lower densities in certain areas are
127 associated with sedimentary rocks in basins (Fig. 2d) whose axes lie parallel to the
128 traces of offshore fracture zones[35]. For a more detailed description of our
129 interpretation, see Methods.
130

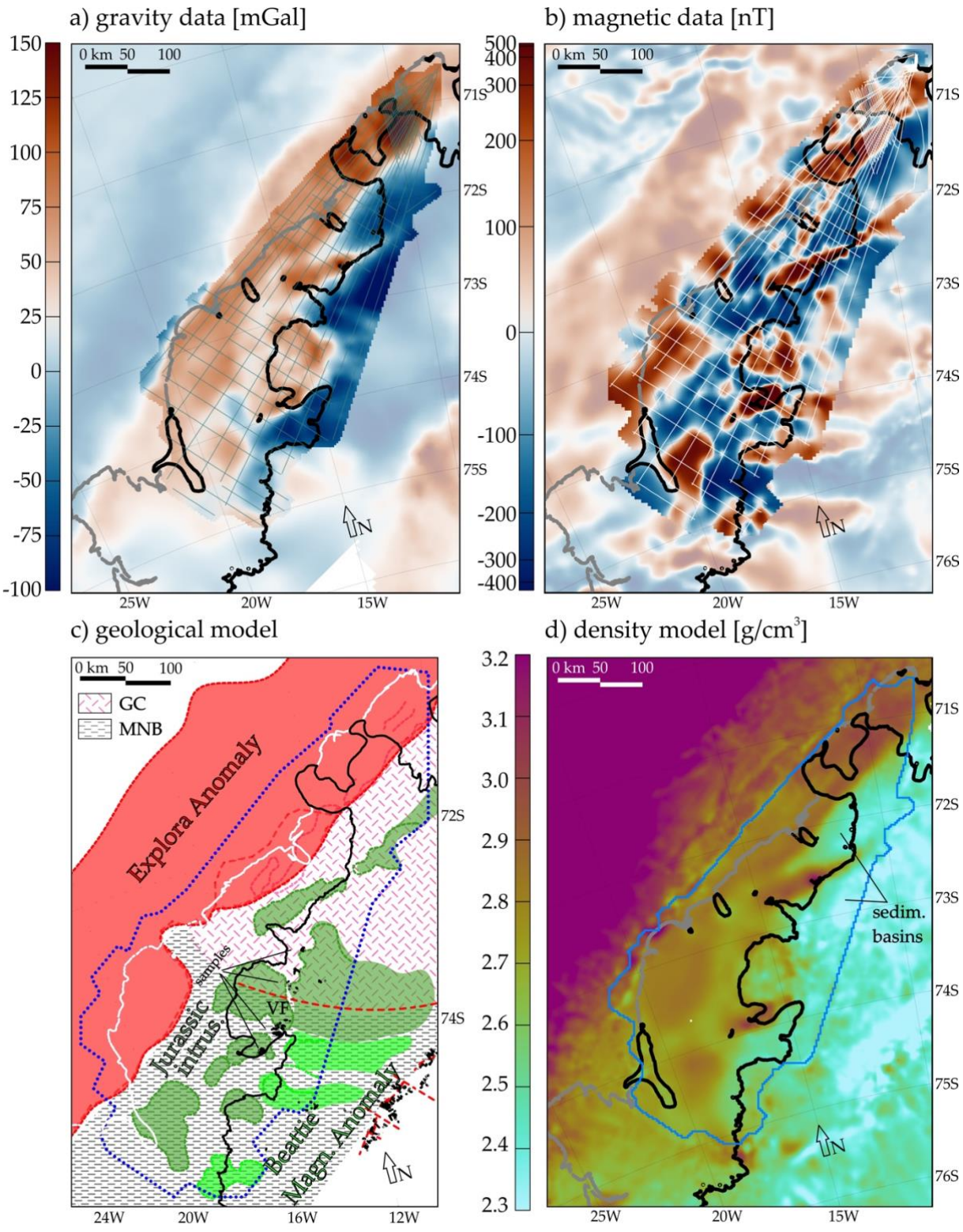

Figure 2: Flight lines, potential field data, geological interpretation, and density model across the Riiser-Larsen Ice Shelf. (a) Newly acquired gravity data (heavy colours) underlain by gravity data compilation AntGG2021[36] (light colours). (b) Newly acquired magnetic data (heavy colours) underlain by the ADMAP-2 compilation[37] (light colours). Flight line segments used for the new grids are shown in grey.

(c) Geological interpretation of the survey area, as inferred from outcrop samples[32] (black) and potential field data (a, b). GC, Grunehogna Craton; MNB, Maud-Natal Belt; VF, Vestfjella. (d) Bedrock density model based on a first inversion towards densities in areas of known topography and on our geological interpretation in (c) in areas of unknown topography. Blue outline: extent of newly acquired gravity data in (a). Calving fronts and grounded areas are extracted from MEaSUREs data collection[18] and additional databanks[19].

Glacial troughs and sub-ice shelf bathymetry

The bathymetric model is shown with contours in Fig. 1 and with neighbouring ice shelves of Dronning Maud Land and Coats Land in Fig. 3. A detailed map is given in the Supplementary Information, together with the resulting water column thickness (Supplementary Figs. 1 & 2). Grounded parts of the ice shelf[18,38] are complemented here by one previously undescribed area of grounding in the eastern part of the ice shelf fed by the Eastern Riiser-Larsen Glacier (labelled here as pinning point 4; Fig. 1). This point was suggested during the bathymetric model generation and is supported by surface changes in the digital elevation model REMA[39,40], as well as base ice signature changes in our ice penetrating radar data (Supplementary Fig. 3).

The updated bathymetry for the Riiser-Larsen Ice Shelf reveals considerable seabed relief under the ice shelves, where the IBCSOV2 bathymetric compilation shows smooth, interpolated bathymetry, complemented only by manually inserted steering points[20] (Supplementary Fig. 4). Our model is 67.2 m deeper on average with a standard deviation of 157 m, and a maximum depth change of -830 m. A comparison

159 to Bed_AntGG2022[31] shows a mean difference of 12 m with a standard deviation of 183
160 m and maximum deviations of ±700 m. Illustrating the effects of our geological
161 interpretation, Bed_AntGG2022 shows shallower depths in the ice shelf's central
162 region that are associated with high-density material, and greater depths over the
163 lower density sedimentary basins.
164
165 Our new bathymetry reveals the presence of deep gateways across the continental
166 shelf break connecting the open ocean to the Riiser-Larsen and Quar ice shelf cavities
167 (Fig. 1). We define these gateways as local bathymetric saddles within a prominent
168 bathymetric ridge that perches along the continental shelf break (dashed purple line
169 in Fig. 1a). Here, the deepest gateway reaches ~520 m depth (Fig. 4a) and is located
170 beneath the central segment of the Riiser-Larsen Ice Shelf at the Vestkapp, where the
171 ice shelf overhangs the underlying continental shelf break (Fig. 1a). We identify four
172 additional gateways to the Riiser-Larsen cavity with water depths exceeding 300 m
173 (Fig. 1) and one gateway to the Quar cavity with 400 m depth (Fig. 1).
174
175 Generally, the uncovered bathymetry shows patterns that can be related to erosional
176 and depositional processes, as is typical of subglacial bathymetry modelled beneath
177 neighbouring ice shelves[24,29,34,41] (Fig. 3). The bathymetric ridge on the continental shelf
178 break – only interrupted by distinct gateways – is consistent with the formation of
179 moraines during extreme advances of grounded ice during the Last Glacial
180 Maximum[42–44].

Shoreward of the continental shelf break, onshore troughs routing fast-flowing glaciers can be observed to continue out over the cavity floor (Figs. 1 & 3), consistent with past erosion by thicker grounded ice to an advanced grounding line. Locally, the troughs are crossed by ridge-like highs oriented perpendicular to ice flow (Figs. 3 & 4a), interpretable as moraines. The trough hosting the Riiser-Larsen Ice Shelf's largest feeder glacier, Veststraumen (Fig. 1), extends for almost 200 km across the cavity floor beyond the grounding line, where it reaches depths of more than 1400 m (Fig. 4a). It connects the grounding line at the Veststraumen inlet to the major bathymetric gateway at the Vestkapp (Fig. 4a).

This trough is flanked onshore and offshore by topographic highs that coincide with prominent magnetic anomalies interpreted as being of magmatic origin (Figs. 1 & 2). Evidently, grounded ice flow has been and continues to be steered by geological contrasts, exploiting weaker metamorphic rocks and/or sedimentary rocks between the magmatic structures. Near the centre line of the cavity, the trough is interrupted at a bathymetric high (bh, Figs. 1 & 3) that is aligned perpendicular to ice flow. This high shows no magnetic response (Fig. 2b) and is likely of depositional character, possibly comprising an ancient grounding line wedge. Other troughs can also be observed to extend out over the cavity floor from beneath the Plogbreen Glacier and, to a lesser extent, the Eastern Riiser-Larsen Glacier (Figs. 1 & 3). The adjacent Quar Ice Shelf hosts a single trough continuation of its own.

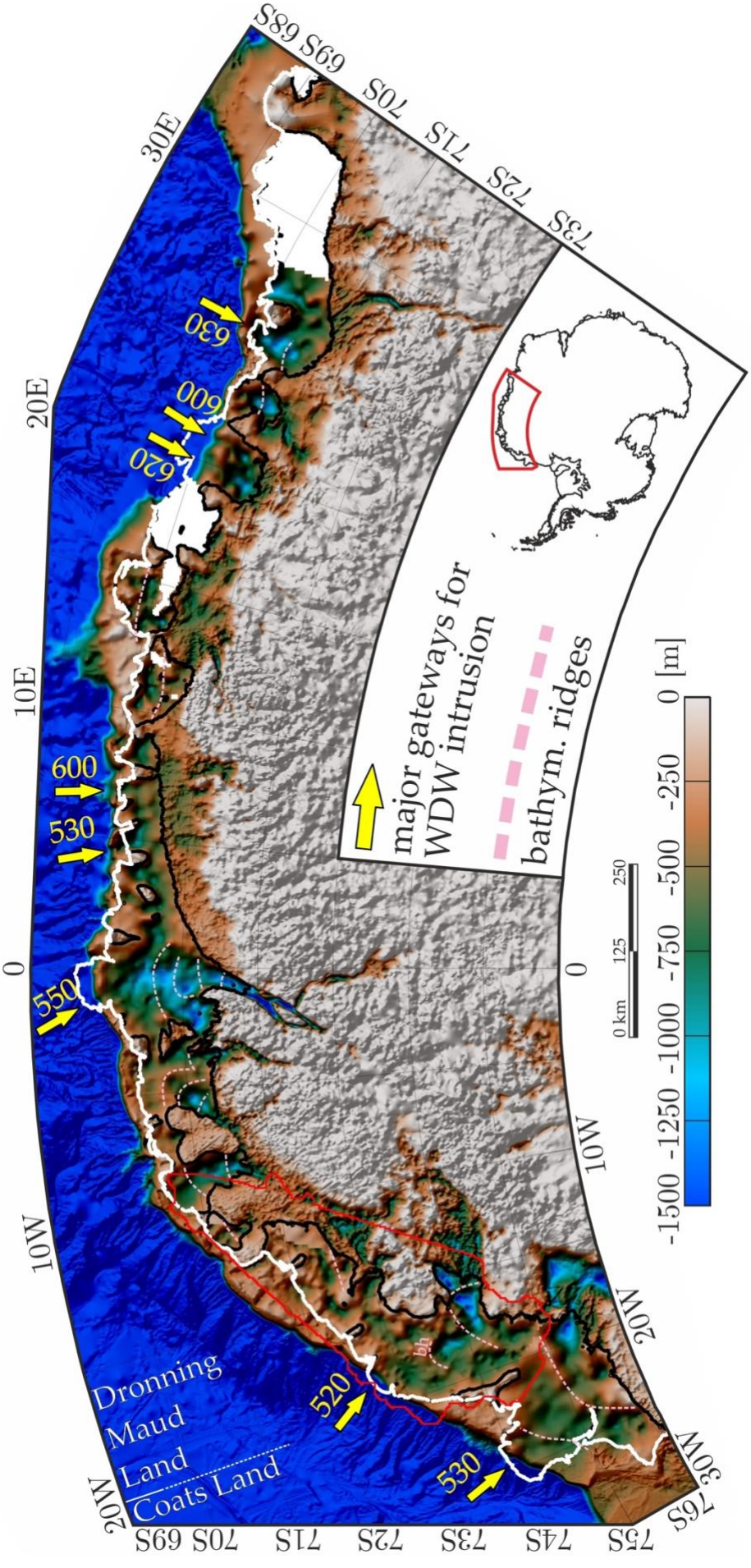
major gateways for WDW intrusion
bathym. ridges
630
600
620
600
530
550
520
530
Dronning Maud Land
Coats Land
0 km 125 250
0 [m] -250 -500 -750 -1000 -1250 -1500
30E 20E 10E 0 10W 20W 30W
68S 69S 70S 71S 72S 73S 74S 75S 76S

Figure 3. Compilation of available topographic information along the Coats Land and Dronning Maud Land coast from this study (red outline), together with other high-resolution gravity-based bathymetric models[24,29,34,41], and compilations[20,21]. Major cavity gateways are shown with yellow arrows at the Stancomb-Wills Ice Tongue (SWIT), Riiser-Larsen, Fimbulisen, Borchgrevink, and Roi Baudouin ice shelves. Transverse troughs and bathymetric ridges (redrawn with pink dashed lines) record a history of ice sheet advances and retreats across the continental shelf. Calving fronts in white and grounding lines in black are extracted from MEaSUREs data collection[18].

Interactions of ice, ocean, and bed

The hydrography at the shelf break, specifically the depth of the thermocline that separates the cold surface waters from the warm WDW below, compared to gateway depth, controls the availability of heat for basal melting at the Riiser-Larsen and Quar ice shelves. To assess potential oceanic impacts on ice shelf stability, we compiled available oceanographic profile data from the World Ocean Database[15], animal-borne data[45], and additional shipborne cruises[13] (Supplementary Fig. 5). We also use four-year-long temperature records from mooring M3[17] (738 m isobath), close to the onset of the Filchner Trough (see Fig. 1 inset for location).

At the continental shelf break, the shallowest depths at which WDW is found in individual oceanographic profiles range roughly between 200 and 800 m depth (Figs. 1a & 4). The mooring data located at the shelf break downstream of the survey area (Fig. 1), records WDW at depths as shallow as about 350 m (Figs. 1c & 4b). The presence

227 of multiple bathymetric gateways along the continental shelf at comparable and even
228 greater depths (Fig. 1) indicates that WDW has access to the ice shelf cavities in this
229 region.
230
231 WDW intrusion into the Riiser Larsen ice shelf cavity at the Vestkapp (VK, Figs. 1 & 3)
232 is probable via the deepest (520 m) gateway in the shelf break ridge (Figs. 1 & 4a).
233 WDW above this depth is observed at the mooring for more than 40% of the time,
234 indicating that persistent inflows of relatively warm water may occur at this location.
235 At the shallower gateways of Riiser-Larsen and Quar with depths ranging from 310 to
236 410 m, WDW intrusions are expected to be more intermittent. Individual
237 oceanographic profiles still show shallower thermocline depths near those locations
238 (Figs. 1a & 4b). Generally, the mooring data and profiles consistently show a shallower
239 thermocline during the austral summer, which is consistent with previous findings of
240 a seasonal inflow onto the continental shelf downstream in the Filchner Trough
241 region[46,47]. However, observations from the neighbouring Fimbulisen ice shelf cavity
242 show that the intermittency of warm inflows deviate from the regular seasonality that
243 is observed at the shelf break[14], possibly due to interactions of the ice shelf tongue that
244 overhangs the continental slope in a similar configuration as is found for the main
245 Vestkapp gateway at the Riiser Larsen ice shelf.
246
247 WDW that enters the cavity at this location can follow a continuous trough all the way
248 to the grounding line of Veststraumen (Fig. 4a), thus promoting an increased thermal

249 forcing in this central part. Higher basal melt rates derived from satellite altimetry
250 data[5] beneath this area of the Riiser-Larsen Ice Shelf and the outlet of the Veststraumen
251 (Fig. 1) are consistent with this interpretation. Here, too, thinner ice associated with
252 basal channels are observed in the ice penetrating radar data (Supplementary Fig. 6).
253 The channels reach heights of up to 300 m above their banks, but become smaller
254 downstream, and are additionally distorted by pinning point 1 (Supplementary Fig.
255 7). Recent, high-resolution modelling showed how already small intrusions of WDW
256 promote differential melt and channel growth in such environments (Zhou et al,
257 submitted), while the origin of these channels could be attributed to subglacial
258 meltwater transported from upstream of the grounding line, as proposed for the Roi
259 Baudouin Ice Shelf[48]. In contrast to these channels and at the westernmost edge of the
260 ice shelf, the absence of radar echo and satellite altimetry[5] independently imply marine
261 ice formation (Supplementary Fig. 8).
262
263 To quantify the impacts of the refined bathymetry on the thermal forcing for the Riiser-
264 Larsen Ice Shelf, we adapted a metric called the Highest Unconnected Isobath (HUB)[49].
265 The HUB quantifies the shallowest depth that offshore waters must rise to in order to
266 reach each point of the grounding line. In combination with averaged offshore
267 hydrographic profiles, HUB can give an estimate of the mean thermal forcing for
268 individual ice shelves[49]. The average HUB in the Riiser-Larsen cavity increases from
269 294 m with BedMachine Antarctica V3[50] to 316 m using our new bathymetry. The
270 maximum HUB depth however increases more drastically, from 380 m to 520 m. This

leads to an increase of 25 % in thermal forcing for the whole ice shelf. The results underline that without accurate knowledge of the bathymetry, oceanic modelling studies focussing on basal melt rates will inevitably misjudge the contribution made by warm waters residing at intermediate depths, such as WDW or Circumpolar Deep Water.

The Riiser-Larsen and Quar ice shelves have both been assessed as stable because they are exposed to relatively cold oceanic forcing. Observations of increased snowfall in the region in recent years[51,52], limited basal melt[5], and limited grounding line migration[53] are consistent with observations that suggest these ice shelves may be gaining mass or at least preserving their mass[5] along with the ice sheet catchments they currently buttress[54–57].

Our new bathymetric model, however, reveals the existence of relatively deep (up to 520 m) gateways connecting the ice shelf cavity to the open ocean, suggesting that even a relatively modest shallowing of the WDW layer may threaten the future stability of the Riiser-Larsen Ice Shelf. Signs that such a change may occur as a consequence of ongoing warming climate are emerging. These include a shift towards warmer and more frequent inflow into the Fimbulisen ice shelf since 2016[58], a sudden warming above the upper part of the continental shelf 390 km west of the study area[16], and shoaling and increased temperatures of warm waters all along the East Antarctic

margin[59]. What is more, a sustained continuation of large-scale sea ice minima[60] could see warmer and less saline surface waters promote the uplift of WDW in winter[13].

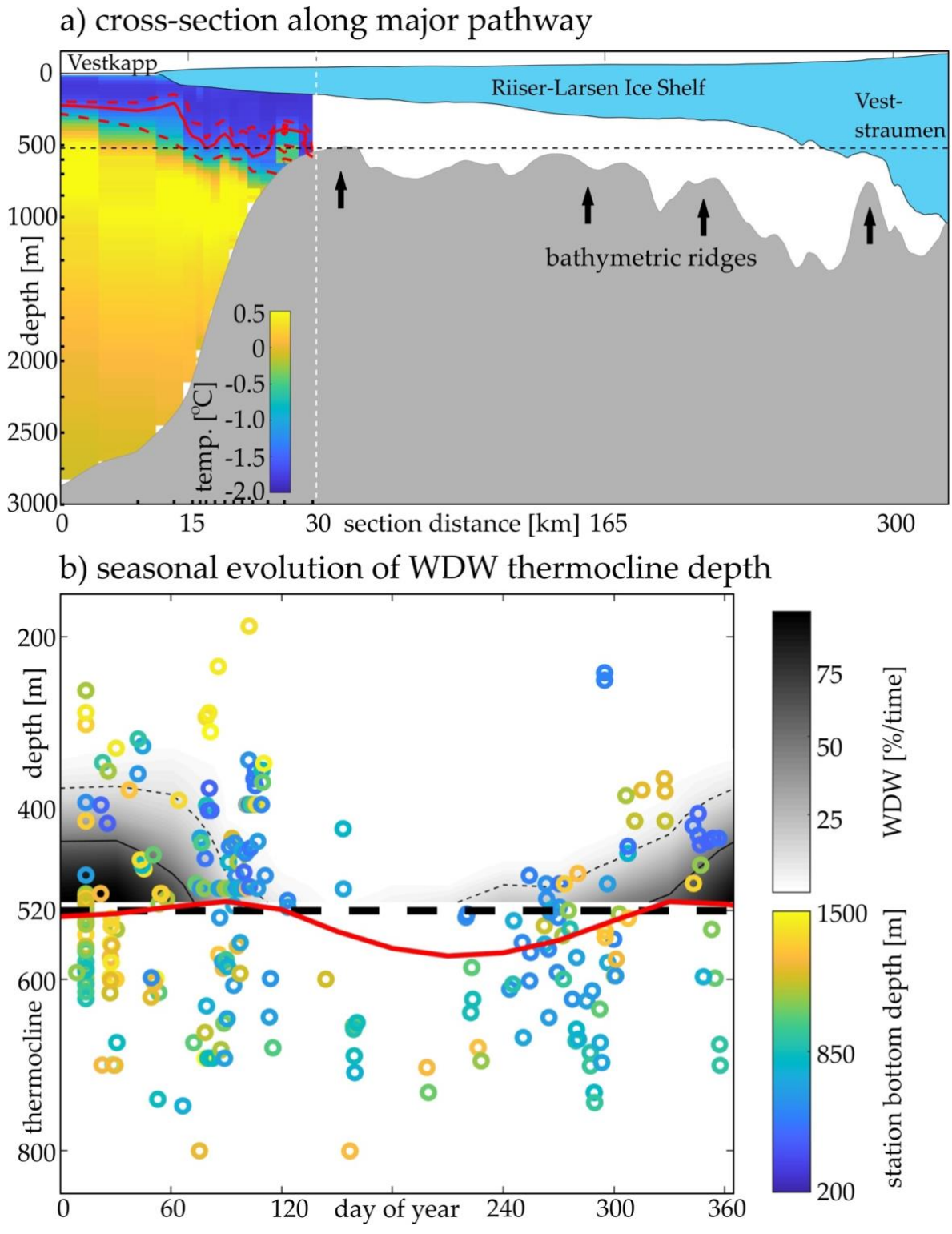

296 **Figure 4.** Oceanographic profiles along the Veststraumen outlet and their seasonal changes along the
297 entire continental shelf. (a) Slope front structure, shelf break and ice shelf cavity geometry along the
298 potential pathway indicated in Fig. 1a. Colour shading shows ocean temperature from hydrographic
299 profiles averaged in bins of isobaths as indicated by black tick marks. The solid (dashed) red contour
300 indicates the average depth (variance) of the -1.5 ºC isotherm relative to the sill depth (dashed black
301 line). Note the different horizontal scales along the transect (left and right of the dashed white vertical
302 line). (b) Seasonal evolution (red contour) of thermocline depth as inferred from 265 hydrographic
303 profiles (coloured rings) taken along the continental shelf break with water depths of 1500 m or
304 shallower (see Fig 1a for locations). The sill depth of the major gateway (dashed black line) is shown as
305 a reference. Gray shading indicates the relative frequency of occurrence of WDW at mooring M3 (see
306 inset in Fig. 1 for location) with solid (dashed) contours indicating the depth at which 50 % (10 %) of all
307 measurements are -1.5 ºC or warmer.
308
309 ***Implications for interactions of the Weddell Gyre with coastal ice shelves***
310 Over the last five years, large areas of the Antarctic margin of Coats Land and
311 Dronning Maud Land (30°W to 35°E) that had previously been mapped only by long
312 distance interpolations have come to be mapped in their entirety by a combination of
313 hydroacoustic[20], seismic[22], radar[21], and gravity-inversion techniques[24,29,31,34,41] (Fig. 3).
314 The coastal topography here strongly indicates that the Dronning Maud Land sector
315 of the East Antarctic Ice Sheet may be fundamentally volatile and may experience large
316 sudden changes in response to minimal shifts within the oceanographic regime.
317
318 A ~2500 km-long shallow ridge along the continental shelf break (Fig. 3) is interrupted
319 by multiple narrow gateways with depths exceeding 500 m. Much like the Riiser-

Larsen Ice Shelf's Vestkapp gateway, these gateways mark the projections of transverse troughs (Fig. 3) that trace the paths of major ice flows during times with thicker ice[29]. For the most part, these gateways are presently too shallow to permit continuous intrusion and exchange of WDW into the cavities. Seasonal intrusions, however, have been observed or postulated for gateways at the Fimbulisen[34,58,61], Borchgrevink, Roi Baudouin[29], and now Riiser-Larsen ice shelves (Fig. 3). An oceanographic regime shift with shoaling thermocline depths could see an increase of WDW intrusions at these ice shelves and the impairment of further ice shelves. This is potentially of regional significance for the broad (up to 200 km) swath of the East Antarctic ice sheet in Dronning Maud Land whose bed depth and landward slope put it at risk of marine ice sheet instability[18,50].

Assessing present and future interactions with the ocean is not just vital for the ice shelves in Dronning Maud and Coats Land. Along-shelf transport via the Weddell Gyre indicate that these ice shelves also play a role in determining the properties of the water that enters Antarctica's largest ice shelf system, Filchner-Ronne[62]. Here, bottom water is produced that plays a crucial role in maintaining the global meridional overturning circulation[63,64]. Currently, oceanographic models concentrating on this sector or the Weddell Sea in general[65,66] are forced to disregard the Riiser- Larsen Ice Shelf and adjacent ice shelves because of the lack of detailed characterizations of their cavities.

Methods

Airborne survey

The aerogeophysical campaign RIISERBATHY was conducted with Polar 5[67] in the austral summer of 2022/2023 out of the German research base Neumayer-III[68]. It included the acquisition of gravity, magnetic, and ice penetrating radar data across the Riiser-Larsen Ice Shelf, the Quar Ice Shelf, and its surroundings. A total of ~12,500 km of survey lines were flown during eleven flights with approximately 58 hours of total flight time (Fig. 2). The constraints of working from a single distant skiway at Neumayer-III at the far eastern end of the survey area, and over an ice shelf that widens westwards meant that a fan-shaped network of flight paths was planned. This results in a moderate loss of spatial resolution towards the west (Fig. 2). Since no prior bathymetric information is available across the floating parts of the ice shelf, the survey was designed to guarantee plenty of overlap with existing shipborne measurements in the open ocean[20] and ice penetrating radar data onshore and over pinning points[18,19,21] (Fig. 2), where the inversion can be explicitly constrained to honour known depth constraints.

Ice penetrating radar data

The ice penetrating radar system used here operates with a centre frequency of 150 MHz and has been widely utilised in Antarctica since the mid-90s[69,70]. During RIISERBATHY, it was flown in toggle mode, alternately acquiring data with both a

short and a long pulse of 60 and 600 ns. This mode reduces horizontal resolution from ~5 to ~10 m at 76 m/s, compared to operating in single-pulse mode, but allows to map internal layers with its short pulse and ice thicknesses of up to 4000 m with its long pulse[69]. Ice thicknesses across the ice shelves and grounded regions adjacent to them are calculated using travel times and a constant electromagnetic wave speed in ice of 0.168 m/ns, which corresponds to a relative dielectric permittivity of about 3.17[69]. With a picking uncertainty of one range bin and a possible velocity variance of 0.5%, the ice thickness uncertainty amounts to about ±20 m[69].

Supplementary Figure 3 shows the flight lines along which ice penetrating radar data was gathered during the survey, together with the ice base position referenced to the ellipsoid. The topographic boundary of ice/bedrock and ice/ocean inferred from the radar data is used to constrain the bathymetric model described below.

Potential field data

Airborne gravity data acquired during survey flights (Fig. 2a) were gathered with a GT-2A gravity meter. Relative values were tied to a known absolute value at Troll Research Station using a portable LaCoste-Romberg gravity meter. A mean survey speed above ground of 76 m/s combined with a low-pass filter length of 100 s results in a horizontal resolution of 3.8 km. Root mean square errors of crossover residuals after levelling are 2.4 mGal, excluding crossovers with flight height differences of more

than 150 m. Gravity data were also collected using a separate strapdown gravimeter system, returning comparable results to those of the GT-2A that are presented in detail elsewhere (Johann et al, 2025; in review).

The acquisition of airborne magnetic data was carried out with a Scintrex Cs-3 caesium vapour magnetometer mounted in a tail boom. A fuselage-mounted three-component Billingsley TFM 100 fluxgate magnetometer was used for magnetic compensation. Diurnal variations of the magnetic field were recorded at Neumayer-III station and used for correction. Processing of magnetic data was carried out using the geophysical software 'Geosoft Oasis montaj'. The workflow included de-spiking, IGRF and diurnal variation corrections as well as levelling procedures. To simplify the interpretation of magnetic anomalies, the magnetic pattern was transformed by a grid-based reduction to the pole. Additional grid-based filtering techniques were applied to constrain magnetic source bodies and trace lineaments, allowing the interpretation of near-surface geological variations that are accounted for in the density model.

Bathymetric model

The bathymetric model developed in this study is based on an inversion of acquired gravity data, which is complemented by existing and newly acquired depth references across the ice shelf and its surroundings. It is created using the 'GMSYS 3D' toolkit

407 extension within 'Geosoft Oasis montaj'. The model has a horizontal resolution of 2.5
408 km with a model base at 10 km depth.
409
410 The model domain consists of three individual layers. i) a surface layer comprising
411 surface positions from the digital elevation model REMA[39,40] and open ocean from
412 AntGG2021[36], ii) an ice-base layer, inferred and interpolated from our newly acquired
413 ice penetrating radar data and complemented by BedMachine Antarctica V3[50], and iii)
414 a bathymetry/topography layer. The latter layer encompasses bedrock depth of
415 grounded ice, seabed depth beneath the ice shelf, and of the open ocean. In areas of
416 grounded ice, bedrock depth is inferred from the ice-base layer, while shipborne
417 bathymetric data provide a quite detailed picture of the seabed beyond the calving
418 front[20] (Figs. 1 & 3).
419
420 Beneath the ice shelf, the bathymetry is unknown and modelled according to the
421 following work flow. First, a uniform bedrock density of 2.67 g/cm^3 is assumed to
422 arrive at a value for a shift that broadly aligns the calculated and observed gravity
423 anomalies. Next, a preliminary inversion for bedrock density is performed and the
424 inferred densities are extracted at points where the ice-bedrock and ocean-bedrock
425 interfaces are known from auxiliary data. This density model is then complemented
426 manually across the ice shelf (Figs. 2d and Supplementary Fig. 9) according to our
427 geological interpretation given in the following (Fig. 2c).
428

Keeping this enhanced density model then fixed, a second inversion towards bedrock depth is performed during which points with known topography are only allowed to move vertically within a small range, allowing for the possibility that they may not be the best representation of the averaged topography reflected in the larger, smoother, enclosing gravity anomaly. These points are corrected manually to their original values afterwards.

Gravity residuals after this inversion (Supplementary Fig. 10) have a root mean square error of 1.3 mGal with peaks of up to 10 mGal. Combining this maximum error with the crossover-derived error of 2.4 mGal in the gravity data implies a total maximum error of 12.4 mGal. A Bouguer slab calculation with this error value using the density contrast of water (1.028 g/cm^3) and the average bedrock density beneath the ice shelf (2.67 g/cm^3) amounts to a conservative estimate of about 180 m of uncertainty in the bathymetric model. Similarly, errors estimated using a Bouguer slab calculation with lithology-related density variability of 2.45-3.05 g/cm^3 (Supplementary Fig. 9), inferred on the basis of the geological interpretation, lie within an envelope of 146 and 208 m. Either of these uncertainty estimates is consistent with comparisons of gravity inversion results to ground-truth data[8,71] and with estimated errors of other models generated based on gravity inversion.

451 ***Geological interpretation***

452 The geological interpretation of the survey area includes two main basement units: the
453 Grunehogna Craton and the Maud-Natal Belt (Fig. 2c). The craton, a detached
454 fragment of the Kaapvaal Craton of southern Africa[72–74], consists of sporadically
455 exposed 3.1 Ga granitic basement intruded by Mesoproterozoic gabbros and tholeiitic
456 sills and overlain by thick flat-lying Mesoproterozoic volcanosedimentary sequences[75–
457 77]. We mapped the craton based on the relatively weak magnetic susceptibilities of its
458 Mesoproterozoic cover sequence, which broadly lends it a low magnetic intensity
459 signature[78] (Fig. 2b). On the craton's margin, the medium- to high-grade metamorphic
460 rocks of the Maud-Natal Belt are related to the assembly of Rodinia[79]. The belt is
461 characterized by broad high-amplitude linear and craton-parallel magnetic
462 anomalies[78] (Fig. 2b). Relatively subdued gravity anomalies are consistent with the
463 expectation that densities of individual lithologies in these very old crystalline rock
464 associations should not vary greatly (Fig. 2a).

465

466 Onshore within the survey area, the craton and mobile belt are overlain by a Permian
467 sandstone/shale sequence and Jurassic continental flood basalts[80], and cut by dolerite
468 dykes, sills, and gabbroic intrusions. The igneous rocks, which are related to those of
469 the Karoo large igneous province in southern Africa[81–84], raise positive magnetic and
470 gravity anomalies[37,85] (marked green in Fig. 2c). Their emplacement along NE-SW
471 linear trends, parallel to the extended continental margin in the Weddell Sea and
472 subglacial rifts further inland, was a response to lithospheric extension during the

473 breakup of Gondwana[85]. Further offshore along the extended margin itself, breakup
474 saw the effusion of a thick wedge of basaltic lava flows that have been imaged in
475 seismic reflection data[86,87]. The wedge raises a strong magnetic anomaly, the Explora
476 Anomaly (marked red in Fig. 2c), which corresponds with a near-continuous positive
477 gravity anomaly, both of which can be shown to continue into the RIISERBATHY
478 survey area. Based on samples from outcrops, densities in the breakup-related igneous
479 rocks and Explora wedge are expected to be higher than in their surroundings (Fig.
480 2d).
481
482 Two distinct magnetic lows cross the Riiser-Larsen Ice Shelf in correlation with linear
483 negative gravity anomalies. Similar associations have been described further east in
484 coastal Dronning Maud Land close to its extended continental margin. These lows run
485 sub-parallel to oceanic fracture zones further offshore and are interpreted to
486 represent sedimentary basins formed over crustal-scale transfer zones that were active
487 during Gondwana breakup[35,88]. By analogy to this interpretation, we assign relatively
488 low densities, consistent with Archean basement covered by break-up related
489 sedimentary basins, for the potential field lows crossing our survey area (Fig. 2c).
490
491 Positive magnetic anomalies SW of Vestfjella may represent the eastward continuation
492 of the Beattie Magnetic Anomaly in southern Africa based on a tight fit Gondwana
493 reconstruction[89,90] (Fig. 2c). The Beattie anomaly may either be related to a magnetite
494 enrichment in granitic basement[91] or to a partly mineralized massive sulfide-magnetite

ore deposit[92]. However, neither the Beattie Magnetic Anomaly nor its Antarctic counterpart has a significant gravity expression. Hence, density in this area is assumed constant, and extrapolated from nearby grounded areas.

Oceanographic data analysis

The oceanographic data compilation (Supplementary Fig. 5) consists of oceanographic profiles extracted from the World Ocean Database[15]. This includes high- and low-resolution CTD (Conductivity, Temperature, and Depth) profiles, Profiling Floats (PFL), Expendable Bathythermographs (XBT), Mechanical Bathythermographs (MBT), and Ocean Station Data (OSD). It is complemented by the latest compilation of oceanographic profiles acquired by instrumented mammals[45] and by additional oceanographic data from Norwegian Antarctic Research Expeditions[13]. A total of 4384 oceanographic stations are compiled in the extent of our survey region (Supplementary Fig. 5): 535 CTD profiles; 3272 mammal-borne profiles or measurements; 125 XBT profiles; 101 MBT profiles; 79 PFL profiles; and 272 OSD profiles. Stations with poor data quality or positioning have been excluded here. The data set includes data from 1959 until early 2023. We defined WDW to lie upwards of a potential density anomaly of 27.65 kg/m^3 and above a temperature of -1.5°C within our oceanographic data compilation (Supplementary Fig. 5). The resulting 1198 thermocline encounters are mapped in the main manuscript (Fig. 1a).

517 Mooring M3 (29.908W, 74.55S) was deployed at 738 m bottom depth just east of the
518 Filchner Trough opening in the southern Weddell Sea. The temperature was recorded
519 between February 2017 and February 2021[17] with an initial vertical resolution of 25 m
520 and a temporal resolution of 1h. The record was interpolated linearly onto a grid with
521 1 m resolution and the depth of the -1.5°C isotherm was inferred at hourly intervals to
522 generate Fig. 1c.
523
524
525 **Data Availability**
526 The bathymetric model, gravity data, magnetic data, and ice penetrating radar data
527 are available at Pangaea. (To reviewers: Pangaea uploads are currently under
528 mortarium until the paper is accepted. Temporary links are shared with the editor in
529 the cover letter. Please get in contact with the editor, if these are not shared with you).
530 Auxiliary topographic data sets are REMA DEM V2
531 (https://doi.org/10.7910/DVN/EBW8UC), BedMachine Antarctica V3
532 (https://nsidc.org/data/nsidc-0756/versions/3), IBCSO V2
533 (https://doi.org/10.1594/PANGAEA.937574), Bed_AntGG2022
534 (https://datadryad.org/dataset/doi:10.5061/dryad.rbnzs7hkc), and BEDMAP3
535 (https://www.bas.ac.uk/project/bedmap/). Grounding line and calving front positions
536 are extracted from the National Snow and Ice Data Center at
537 https://nsidc.org/data/nsidc-0498/versions/2. The position of additional ice rises and
538 rumples[19], as well as ice flow vectors[93] are available. Oceanographic data is extracted

539 from the World Ocean Database (https://www.ncei.noaa.gov/products/world-ocean-
540 database), and additional CTD data[13]. Part of the marine mammal data were collected
541 and made freely available by the International MEOP Consortium and the national
542 programs that contribute to it (http://www.meop.net). The mooring data from M3 are
543 available at Pangaea (https://doi.pangaea.de/10.1594/PANGAEA.962043).
544
545
546 ## Acknowledgements
547 We thank the logistical and aircraft technical staff at AWI, Neumayer-III, and
548 Norwegian Troll Research Station for their support during the 'RIISERBATHY'
549 campaign. The airborne campaign was jointly funded by AWI within grant
550 AWI_PA_02138 and BGR as part of the GEA programme (Geodynamical Evolution of
551 East Antarctica). The authors are also grateful to the Kenn Borek Air crew for their
552 dedication and professionalism. The authors would like to thank Aspen Technology,
553 Inc. for providing software licenses and support. HE is funded by the AWI INSPIRES
554 programme. TH was supported by the Research Council of Norway through the
555 Centre for ice, Cryosphere, Carbon and Climate, project 332635. A research stay of HE
556 at the Norwegian Polar Institute with TH and KM was funded by PROCEED.
557
558
559 ## Author Contributions
560 HE, GE, AR, and AL devised the study. HE and GE conducted the airborne campaign.

HE processed GT-2A gravity data, while FJ and SL provided input for gravity data analysis. HE, VH, and DS processed ice penetrating radar data. AR, AL, and GE processed magnetic data and interpreted it towards the geological setting. HE compiled topographic information and developed the bathymetric model. HE, KM, and SF analysed ice penetrating radar data and interpreted it regarding ice-ocean interactions. HE, TH, and ED compiled and analysed oceanographic data along the calving front and interpreted it regarding ice-ocean interactions. GF calculated thermal forcing from the updated bathymetry. HE, AR, and GE wrote the manuscript with contributions from all co-authors.

Competing Interests

The authors declare no competing interests.

Supporting Information

Extended information for this paper is available online.

References

1. Dupont, T. K. & Alley, R. B. Assessment of the importance of ice-shelf buttressing to ice-sheet flow: buttressing sensitivity. *Geophys. Res. Lett.* **32**, (2005).

583 2. Rignot, E. Observations of grounding zones are the missing key to understand ice melt
584 in Antarctica. *Nat. Clim. Chang.* **13**, 1010–1013 (2023).
585 3. Dinh, A., Rignot, E., Mazloff, M. & Fenty, I. Southern Ocean High-Resolution (SOhi)
586 Modeling Along the Antarctic Ice Sheet Periphery. *Geophys. Res. Lett.* **51**, e2023GL106377
587 (2024).
588 4. DeConto, R. M. & Pollard, D. Contribution of Antarctica to past and future sea-level
589 rise. *Nature* **531**, 591–597 (2016).
590 5. Davison, B. J. *et al.* Annual mass budget of Antarctic ice shelves from 1997 to 2021.
591 *Science Advances* **9**, eadi0186 (2023).
592 6. Jenkins, A. *et al.* Observations beneath Pine Island Glacier in West Antarctica and
593 implications for its retreat. *Nat Geosci* **3**, 468–472 (2010).
594 7. Tinto, K. J. *et al.* Ross Ice Shelf response to climate driven by the tectonic imprint on
595 seafloor bathymetry. *Nat. Geosci.* **12**, 441–449 (2019).
596 8. Greenbaum, J. S. *et al.* Ocean access to a cavity beneath Totten Glacier in East
597 Antarctica. *Nat Geosci* **8**, 294–298 (2015).
598 9. Andreasen, J. R., Hogg, A. E. & Selley, H. L. Change in Antarctic ice shelf area from
599 2009 to 2019. *The Cryosphere* **17**, 2059–2072 (2023).
600 10. Park, Y., Charriaud, E., Craneguy, P. & Kartavtseff, A. Fronts, transport, and Weddell
601 Gyre at 30°E between Africa and Antarctica. *J. Geophys. Res.* **106**, 2857–2879 (2001).
602 11. Vernet, M. *et al.* The Weddell Gyre, Southern Ocean: Present Knowledge and Future
603 Challenges. *Rev. Geophys.* **57**, 623–708 (2019).
604 12. Reeve, K. A. *et al.* A gridded data set of upper-ocean hydrographic properties in the
605 Weddell Gyre obtained by objective mapping of Argo float measurements. *Earth Syst. Sci.*
606 *Data* **8**, 15–40 (2016).
607 13. Hattermann, T. Antarctic Thermocline Dynamics along a Narrow Shelf with Easterly
608 Winds. *Journal of Physical Oceanography* **48**, 2419–2443 (2018).

609 14. Lauber, J., Hattermann, T., De Steur, L., Darelius, E. & Fransson, A. Hydrography
610 and circulation below Fimbulisen Ice Shelf, East Antarctica, from 14 years of moored
611 observations. *Ocean Sci.* **20**, 1585–1610 (2024).
612 15. Boyer, T. P. *et al.* World Ocean Database 2018.
613 16. Darelius, E., Dundas, V., Janout, M. & Tippenhauer, S. Sudden, local temperature
614 increase above the continental slope in the southern Weddell Sea, Antarctica. *Ocean Sci.* **19**,
615 671–683 (2023).
616 17. Darelius, E., Janout, M. A., Fer, I. & Sallée, J.-B. Physical oceanography and current
617 velocity data from mooring M3 on the upper continental slope, east of Filchner Trough,
618 February 2017 – February 2021. https://doi.pangaea.de/10.1594/PANGAEA.962043 (2023)
619 doi:10.1594/PANGAEA.962043.
620 18. Mouginot, J., Rignot, E. & Scheuchl, B. MEaSUREs Antarctic Grounding Line from
621 Differential Satellite Radar Interferometry, Version 2 [Data Set]. Boulder, Colorado USA.
622 NASA National Snow and Ice Data Center Distributed Active Archive Center.
623 https://doi.org/10.5067/IKBWW4RYHF1Q (2016).
624 19. Moholdt, G. & Matsuoka, K. Inventory of Antarctic ice rises and rumples (version 1)
625 [Dataset]. Norwegian Polar Institute. NPOLAR
626 https://doi.org/10.21334/NPOLAR.2015.9174E644 (2015).
627 20. Dorschel, B. *et al.* The International Bathymetric Chart of the Southern Ocean Version
628 2. *Sci Data* **9**, 275 (2022).
629 21. Morlighem, M. *et al.* Deep glacial troughs and stabilizing ridges unveiled beneath the
630 margins of the Antarctic ice sheet. *Nat. Geosci.* **13**, 132–137 (2020).
631 22. Frémand, A. C. *et al.* Antarctic Bedmap data: Findable, Accessible, Interoperable, and
632 Reusable (FAIR) sharing of 60 years of ice bed, surface, and thickness data. *Earth Syst. Sci.*
633 *Data* **15**, 2695–2710 (2023).
634 23. Smith, E. C. *et al.* Detailed Seismic Bathymetry Beneath Ekström Ice Shelf,

635 Antarctica: Implications for Glacial History and Ice-Ocean Interaction. *Geophys. Res. Lett.*
636 **47**, (2020).
637 24. Hodgson, D. A. *et al.* Past and future dynamics of the Brunt Ice Shelf from seabed
638 bathymetry and ice shelf geometry. *The Cryosphere* **13**, 545–556 (2019).
639 25. Tinto, K. J. & Bell, R. E. Progressive unpinning of Thwaites Glacier from newly
640 identified offshore ridge: Constraints from aerogravity. *Geophys. Res. Lett.* **38**, n/a-n/a (2011).
641 26. Cochran, J. R., Jacobs, S. S., Tinto, K. J. & Bell, R. E. Bathymetric and oceanic
642 controls on Abbot Ice Shelf thickness and stability. *The Cryosphere* **8**, 877–889 (2014).
643 27. Muto, A. *et al.* Subglacial bathymetry and sediment distribution beneath Pine Island
644 Glacier ice shelf modeled using aerogravity and in situ geophysical data: New results. *Earth*
645 *and Planetary Science Letters* **433**, 63–75 (2016).
646 28. Constantino, R. R. & Tinto, K. J. Cook Ice Shelf and Ninnis Glacier Tongue
647 Bathymetry From Inversion of Operation Ice Bridge Airborne Gravity Data. *Geophys. Res.*
648 *Lett.* **50**, e2023GL103815 (2023).
649 29. Eisermann, H., Eagles, G., Ruppel, A. S., Läufer, A. & Jokat, W. Bathymetric Control
650 on Borchgrevink and Roi Baudouin Ice Shelves in East Antarctica. *J. Geophys. Res. Earth*
651 *Surf.* **126**, (2021).
652 30. Scheinert, M. *et al.* New Antarctic gravity anomaly grid for enhanced geodetic and
653 geophysical studies in Antarctica. *Geophys. Res. Lett.* **43**, 600–610 (2016).
654 31. Charrassin, R., Millan, R., Rignot, E. & Scheinert, M. Bathymetry of the Antarctic
655 continental shelf and ice shelf cavities from circumpolar gravity anomalies and other data. *Sci*
656 *Rep* **15**, 1214 (2025).
657 32. Cox, S. C. *et al.* A continent-wide detailed geological map dataset of Antarctica. *Sci*
658 *Data* **10**, 250 (2023).
659 33. Jokat, W. *et al.* The continental margin off East Antarctica between 10°W and 30°W.
660 *Geological Society, London, Special Publications* **108**, 129–141 (1996).

661 34. Eisermann, H., Eagles, G., Ruppel, A., Smith, E. C. & Jokat, W. Bathymetry Beneath
662 Ice Shelves of Western Dronning Maud Land, East Antarctica, and Implications on Ice Shelf
663 Stability. *Geophys. Res. Lett.* **47**, (2020).
664 35. Eagles, G. & Eisermann, H. The Skytrain plate and tectonic evolution of southwest
665 Gondwana since Jurassic times. *Sci Rep* **10**, 19994 (2020).
666 36. Scheinert, M., Zingerle, P., Schaller, T. & Pail, R. Antarctic gravity anomaly and
667 height anomaly grids (AntGG2021). PANGAEA https://doi.org/10.1594/PANGAEA.971238
668 (2024).
669 37. Golynsky, A. V. *et al.* New Magnetic Anomaly Map of the Antarctic. *Geophys. Res.*
670 *Lett.* **45**, 6437–6449 (2018).
671 38. Matsuoka, K. *et al.* Antarctic ice rises and rumples: Their properties and significance
672 for ice-sheet dynamics and evolution. *Earth-Science Reviews* **150**, 724–745 (2015).
673 39. Howat, I. M., Porter, C., Smith, B. E., Noh, M.-J. & Morin, P. The Reference
674 Elevation Model of Antarctica. *The Cryosphere* **13**, 665–674 (2019).
675 40. Howat, I., Porter, C., Smith, B. E., Noh, M.-J. & Morin, P. The Reference Elevation
676 Model of Antarctica – Mosaics, Version 2. Harvard Dataverse, V1
677 https://doi.org/10.7910/DVN/EBW8UC (2022).
678 41. Eisermann, H., Eagles, G. & Jokat, W. Coastal bathymetry in central Dronning Maud
679 Land controls ice shelf stability. *Sci Rep* **14**, 1367 (2024).
680 42. Grobe, H. & Mackensen, A. Late Quaternary Climatic Cycles as Recorded in
681 Sediments from the Antarctic Continental Margin. in *Antarctic Research Series* (eds. Kennett,
682 J. P. & Warkne, D. A.) 349–376 (American Geophysical Union, Washington, D. C., 1992).
683 doi:10.1029/AR056p0349.
684 43. Hillenbrand, C.-D. *et al.* Reconstruction of changes in the Weddell Sea sector of the
685 Antarctic Ice Sheet since the Last Glacial Maximum. *Quaternary Science Reviews* **100**, 111–
686 136 (2014).

687 44. Suganuma, Y. *et al.* Regional sea-level highstand triggered Holocene ice sheet
688 thinning across coastal Dronning Maud Land, East Antarctica. *Commun Earth Environ* **3**, 1–
689 11 (2022).
690 45. Roquet, F. *et al.* Estimates of the Southern Ocean general circulation improved by
691 animal-borne instruments. *Geophys. Res. Lett.* **40**, 6176–6180 (2013).
692 46. Ryan, S., Hattermann, T., Darelius, E. & Schröder, M. Seasonal cycle of hydrography
693 on the eastern shelf of the Filchner Trough, Weddell Sea, Antarctica. *J. Geophys. Res. Oceans*
694 **122**, 6437–6453 (2017).
695 47. Årthun, M., Nicholls, K. W., Makinson, K., Fedak, M. A. & Boehme, L. Seasonal
696 inflow of warm water onto the southern Weddell Sea continental shelf, Antarctica. *Geophys.*
697 *Res. Lett.* **39**, (2012).
698 48. Drews, R. *et al.* Actively evolving subglacial conduits and eskers initiate ice shelf
699 channels at an Antarctic grounding line. *Nat Commun* **8**, 15228 (2017).
700 49. Finucane, G. & Stewart, A. L. A Predictive Theory for Heat Transport Into Ice Shelf
701 Cavities. *Geophys. Res. Lett.* **51**, e2024GL108196 (2024).
702 50. Morlighem, M. MEaSUREs BedMachine Antarctica, Version 3. NASA National
703 Snow and Ice Data Center Distributed Active Archive Center. (2022).
704 51. Thomas, E. R. *et al.* Regional Antarctic snow accumulation over the past 1000 years.
705 *Clim. Past* **13**, 1491–1513 (2017).
706 52. Medley, B. *et al.* Temperature and Snowfall in Western Queen Maud Land Increasing
707 Faster Than Climate Model Projections. *Geophys. Res. Lett.* **45**, 1472–1480 (2018).
708 53. Konrad, H. *et al.* Net retreat of Antarctic glacier grounding lines. *Nat Geosci* **11**, 258–
709 262 (2018).
710 54. Gardner, A. S. *et al.* Increased West Antarctic and unchanged East Antarctic ice
711 discharge over the last 7 years. *The Cryosphere* **12**, 521–547 (2018).
712 55. The IMBIE team. Mass balance of the Antarctic Ice Sheet from 1992 to 2017. *Nature*

713 **558**, 219–222 (2018).
714 56. Gudmundsson, G. H., Paolo, F. S., Adusumilli, S. & Fricker, H. A. Instantaneous
715 Antarctic ice sheet mass loss driven by thinning ice shelves. *Geophys. Res. Lett.* **46**, 13903–
716 13909 (2019).
717 57. Rignot, E. *et al.* Four decades of Antarctic Ice Sheet mass balance from 1979–2017.
718 *Proc. Natl. Acad. Sci. U.S.A.* **116**, 1095–1103 (2019).
719 58. Lauber, J. *et al.* Warming beneath an East Antarctic ice shelf due to increased subpolar
720 westerlies and reduced sea ice. *Nat. Geosci.* **16**, 877–885 (2023).
721 59. Herraiz-Borreguero, L. & Naveira Garabato, A. C. Poleward shift of Circumpolar
722 Deep Water threatens the East Antarctic Ice Sheet. *Nat. Clim. Chang.* **12**, 728–734 (2022).
723 60. Dalaiden, Q. *et al.* An Unprecedented Sea Ice Retreat in the Weddell Sea Driving an
724 Overall Decrease of the Antarctic Sea-Ice Extent Over the 20th Century. *Geophys. Res. Lett.*
725 **50**, e2023GL104666 (2023).
726 61. Hattermann, T., Smedsrud, L. H., Nøst, O. A., Lilly, J. M. & Galton-Fenzi, B. K.
727 Eddy-resolving simulations of the Fimbul Ice Shelf cavity circulation: Basal melting and
728 exchange with open ocean. *Ocean Modelling* **82**, 28–44 (2014).
729 62. Thoma, M., Grosfeld, K. & Lange, M. A. Impact of the Eastern Weddell Ice Shelves
730 on water masses in the eastern Weddell Sea. *J. Geophys. Res.* **111**, C12010 (2006).
731 63. Orsi, A. H., Johnson, G. C. & Bullister, J. L. Circulation, mixing, and production of
732 Antarctic Bottom Water. *Progress in Oceanography* **43**, 55–109 (1999).
733 64. Akhoudas, C. *et al.* Ice Shelf Basal Melt and Influence on Dense Water Outflow in the
734 Southern Weddell Sea. *J. Geophys. Res. Oceans* **125**, e2019JC015710 (2020).
735 65. Hellmer, H. H., Kauker, F., Timmermann, R. & Hattermann, T. The Fate of the
736 Southern Weddell Sea Continental Shelf in a Warming Climate. *J. Climate* **30**, 4337–4350
737 (2017).
738 66. Timmermann, R., Wang, Q. & Hellmer, H. H. Ice-shelf basal melting in a global

739 finite-element sea-ice/ice-shelf/ocean model. *Ann. Glaciol.* **53**, 303–314 (2012).
740 67. Alfred-Wegener-Institut Helmholtz-Zentrum für Polar- und Meeresforschung. Polar
741 aircraft Polar5 and Polar6 operated by the Alfred Wegener Institute. *JLSRF* **2**, A87–A87
742 (2016).
743 68. Alfred-Wegener-Institut Helmholtz-Zentrum für Polar- und Meeresforschung.
744 Neumayer III and Kohnen Station in Antarctica operated by the Alfred Wegener Institute.
745 *JLSRF* **2**, A85–A85 (2016).
746 69. Steinhage, D. Beitrage aus geophysikalischen Messungen in Dronning Maud Land,
747 Antarktis, zur Auffindung eines optimalen Bohrpunktes fÃ¼eine Eiskerntiefbohrung.
748 *Berichte zur Polar-und Meeresforschung* **384**, 116 (2001).
749 70. Nixdorf, U. *et al.* The newly developed airborne radio-echo sounding system of the
750 AWI as a glaciological tool. *Ann. Glaciol.* **29**, 231–238 (1999).
751 71. Brisbourne, A. M. *et al.* Seabed topography beneath Larsen C Ice Shelf from seismic
752 soundings. *The Cryosphere* **8**, 1–13 (2014).
753 72. Halpern, M., Umpierre, M. & Linares, E. Radiometric ages of crystalline rocks from
754 southern South America as related to Gondwana and Andean geologic provinces. in
755 *Proceedings of upper mantle symposium, Buenos Aires IV, Petrologıa y Volcanismo* 345–356
756 (1970).
757 73. Groenewald, P. B., Moyes, A. B., Grantham, G. H. & Krynauw, J. R. East Antarctic
758 crustal evolution: geological constraints and modelling in western Dronning Maud Land.
759 *Precambrian Research* **75**, 231–250 (1995).
760 74. Jones, D. L., Bates, M. P., Li, Z.-X., Corner, B. & Hodgkinson, G. Palaeomagnetic
761 results from the ca. 1130 Ma Borgmassivet intrusions in the Ahlmannryggen region of
762 Dronning Maud Land, Antarctica, and tectonic implications. *Tectonophysics* **375**, 247–260
763 (2003).
764 75. Barton, J. M., Klemd, R., Allsopp, H. L., Auret, S. H. & Copperthwaite, Y. E. The

765 geology and geochronology of the Annandagstoppane granite, Western Dronning Maud Land,
766 Antarctica. *Contr. Mineral. and Petrol.* **97**, 488–496 (1987).
767 76. Marschall, H. R. *et al.* The Annandagstoppane Granite, East Antarctica: Evidence for
768 Archaean Intracrustal Recycling in the Kaapvaal–Grunehogna Craton from Zircon O and Hf
769 Isotopes. *Journal of Petrology* **51**, 2277–2301 (2010).
770 77. Curtis, M. L. & Riley, T. R. Mobilization of fluidized sediment during sill
771 emplacement, western Dronning Maud Land, East Antarctica. *Antartic science* **15**, 393–398
772 (2003).
773 78. Golynsky, A. & Jacobs, J. Grenville-Age versus Pan-African Magnetic Anomaly
774 Imprints in Western Dronning Maud Land, East Antarctica. *The Journal of Geology* **109**,
775 136–142 (2001).
776 79. Läufer, A. Geology and Geodynamic Evolution of Dronning Maud Land, East
777 Antarctica. in *Geology of the Antarctic Continent* 254–295 (Borntraeger Science Publishers,
778 Stuttgart, 2021).
779 80. Hjelle, A. & Winsnes, T. *The Sedimentary and Volcanic Sequence of Vestfjella,*
780 *Dronning Maud Land.* (Universitetsforlaget, 1972).
781 81. Furnes, H., Vad, E., Austrheim, H., Mitchell, J. G. & Garmann, L. B. Geochemistry of
782 basalt lavas from Vestfjella and adjacent areas, Dronning Maud Land, Antarctica. *Lithos* **20**,
783 337–356 (1987).
784 82. Luttinen, A. V. & Furnes, H. Flood Basalts of Vestfjella: Jurassic Magmatism Across
785 an Archaean–Proterozoic Lithospheric Boundary in Dronning Maud Land, Antarctica.
786 *Journal of Petrology* **41**, 1271–1305 (2000).
787 83. Vuori, S. K. & V. Luttinen, A. The Jurassic gabbroic intrusions of Utpostane and
788 Muren: insights into Karoo-related plutonism in Dronning Maud Land, Antarctica. *Antartic*
789 *science* **15**, 283–301 (2003).
790 84. Riley, T. R. *et al.* U–Pb zircon (SHRIMP) ages for the Lebombo rhyolites, South

Africa: refining the duration of Karoo volcanism. *JGS* **161**, 547–550 (2004).

85. Riedel, S., Jacobs, J. & Jokat, W. Interpretation of new regional aeromagnetic data over Dronning Maud Land (East Antarctica). *Tectonophysics* **585**, 161–171 (2013).

86. Jokat, W., Boebel, T., König, M. & Meyer, U. Timing and geometry of early Gondwana breakup: EARLY GONDWANA BREAKUP. *J. Geophys. Res.* **108**, (2003).

87. Jokat, W., Ritzmann, O., Reichert, C. & Hinz, K. Deep Crustal Structure of the Continental Margin off the Explora Escarpment and in the Lazarev Sea, East Antarctica. *Mar Geophys Res* **25**, 283–304 (2004).

88. Ruppel, A., Jacobs, J., Eagles, G., Läufer, A. & Jokat, W. New geophysical data from a key region in East Antarctica: Estimates for the spatial extent of the Tonian Oceanic Arc Super Terrane (TOAST). *Gondwana Research* **59**, 97–107 (2018).

89. Leinweber, V. T. & Jokat, W. The Jurassic history of the Africa–Antarctica corridor — new constraints from magnetic data on the conjugate continental margins. *Tectonophysics* **530–531**, 87–101 (2012).

90. Mieth, M. & Jokat, W. New aeromagnetic view of the geological fabric of southern Dronning Maud Land and Coats Land, East Antarctica. *Gondwana Research* **25**, 358–367 (2014).

91. Corner, B. The Beattie anomaly and its significance for crustal evolution within the Gondwana framework. in *1st SAGA Biennial Conference and Exhibition* cp-222-00006 (European Association of Geoscientists & Engineers, 1989).

92. Lindeque, A., De Wit, M. J., Ryberg, T., Weber, M. & Chevallier, L. Deep crustal profile across the southern Karoo Basin and Beattie Magnetic Anomaly, South Africa: an integrated interpretation with tectonic implications. *South African Journal of Geology* **114**, 265–292 (2011).

93. Mouginot, J., Rignot, E. & Scheuchl, B. MEaSUREs Phase-Based Antarctica Ice Velocity Map, Version 1 [Data Set]. Boulder, Colorado USA. NASA National Snow and Ice

817 Data Center Distributed Active Archive Center. https://doi.org/10.5067/PZ3NJ5RXRH10
818 (2019).
819

Supplementary Files

This is a list of supplementary files associated with this preprint. Click to download.

- SupplementaryInformationEisermannver00.pdf